Detection of shadows in high spatial resolution ocean satellite data using DINEOF

Aida Alvera-Azcárate [a,*], Dimitry Van der Zande [b], Alexander Barth [a],
João Felipe Cardoso dos Santos [b], Charles Troupin [a], Jean-Marie Beckers [a]

[a] *AGO-GHER, University of Liège Allée du Six Aout, 17, Sart Tilman, Liège 4000, Belgium*
[b] *Royal Belgian Institute of Natural Sciences (RBINS), Direction Natural Environment Rue Vautier 29, 1000 Brussels, Belgium*

A B S T R A C T

Cloud shadows present in high spatial resolution remote sensing datasets can affect the quality of the data if they are not properly detected and removed. When working with ocean data, cloud shadows are often difficult to differentiate from non-shadow values, since they show similar spectral characteristics than water pixels. A methodology to detect cloud shadows over the ocean is proposed. The present approach combines a series of tests applied directly to the physical variables derived from the satellite measured radiances, and it therefore does not depend on the wavebands measured by a specific satellite sensor. The tests include a departure from an EOF basis calculated using DINEOF, a threshold test, a proximity to cloud test and a ray tracing test. The weighing of the different tests can be adapted to each case or domain of study. The results are compared to manually detected shadows and to another shadow detection method. The approach works with cloud shadows of all sizes, and also with very small objects shadows, like the shadows projected by offshore windmills.

1. Introduction

The Multispectral Instrument (MSI) onboard Sentinel-2 satellites A and B is mainly designed to provide information on land surfaces for applications in agriculture, geology, forestry, mapping, global change research, etc. However, its performance in terms of signal-to-noise ratio (SNR) is sufficient to be used for marine applications, especially in turbid coastal waters. Compared to the dedicated ocean colour sensors (Moderate Resolution Imaging Spectroradiometer-Aqua -MODIS-AQUA-, Visible Infrared Imaging Radiometer Suite -VIIRS- and Sentinel-3 Ocean and Land Colour Instrument -OLCI) Sentinel-2/MSI offers great advantages in terms of spatial resolution enabling the development of a new generation of coastal water quality products, as high resolution suspended particulate matter (SPM) and chlorophyll-a (CHL).

The presence of clouds limits the usability of Sentinel-2 data, as happens with all optical satellite sensors. A more specific problem encountered by satellite sensors measuring at high spatial resolution, like Sentinel-2/MSI, is the presence of spatially resolved cloud shadows, which partially affect the signal being measured. These cloud shadows appear as border features surrounding clouds, but also as detached features, not associated with pixels identified as clouds. This is the case of shadows resulting from small, scattered clouds like cumulus-type clouds or plane contrails. Given the high spatial resolution of Sentinel-2 data, objects present in the coast or at sea (i.e. offshore windmills)

can cast also small shadows. The shadows from clouds and these objects do not show specific spectral characteristics over water pixels (i.e. the ocean, which is in general a dark surface), which is precisely the object of this study. The intensity of the cloud shadows depends on the thickness of the originating cloud. This makes it very difficult to accurately detect and flag them in order to exclude them from further processing. Furthermore, it is difficult to know the altitude of the different clouds present in a Sentinel-2 satellite image, an information that would allow the location of the shadows by projection. In addition, if a cloud is out of the limits of the domain of study, but projecting a shadow within it, projection approaches can fail.

The presence of shadows therefore decreases the quality of the Sentinel-2 data, and a method to detect them is required. Methods developed to detect shadows in high spatial resolution data, as Landsat data, are based for example on cloud projection (i.e. Zhu and Woodcock, 2012), a combination of projection plus spectral band tests (i.e. Huang et al., 2010; Luo et al., 2008; Braaten et al., 2015; Sun et al., 2018; Zhai et al., 2018), or spectral tests plus temporal coherency tests (Goodwin et al., 2013; Zhu and Woodcock, 2014). An improvement of the spectral plus projection combination test was proposed by Zhu and Woodcock (2014) by adding a temporal dimension to increase the robustness of the results. Methods based on spectral characteristics of an image depend on the existence of specific bands (like a thermal band) and are therefore satellite-dependent. Extensions to these approaches have been proposed

---

* Corresponding author.
E-mail address: a.alvera@ulg.ac.be (A. Alvera-Azcárate).

(i.e. Zhu, Z. and Wang, S. and Woodcock, C.E., 2015; Frantz et al., 2018; Qiu et al., 2019) that work with satellites without thermal band, like Sentinel-2. Another approach is using neural networks to detect cloud shadows (i.e. Hughes and Hayes, 2014), which can provide information on clouds shadows independently on the spectral bands present in a satellite. Most of the mentioned works have been applied to land satellite scenes, and very few deal with cloud shadow detection over the ocean. Detection of cloud shadows over water is challenging because of its dark colour, which results in very similar spectral characteristics to those of cloud shadows. The complexity of cloud top altitude variations makes it very difficult to know at which distance from the cloud the shadows can be actually located. Moreover, the large spatial variability of coastal turbid waters results in a very complex field with correct low SPM values and shadows intermingled in a single image. Temporal variability can be also very high, specially in the presence of strong currents, tidal-induced resuspension of bottom sediments or estuary discharges. This makes also difficult the exploitation of temporal coherency in the time series, specially for data from satellites like Sentinel-2, which have a revisit time of 5 days.

The objective of this work is to derive a shadow detection approach for high resolution sensors like Sentinel-2 over oceanic waters, by performing a series of tests on specific geophysical variables (SPM and CHL in this case) to ensure that the approach can be applied to any sensor, independently of the spectral bands available. The tests include a departure from an Empirical Orthogonal Function (EOF) basis obtained by DINEOF (Data Interpolating Empirical Orthogonal Functions, Beckers and Rixen (2003); Alvera-Azcárate et al. (2005)), as well as a threshold test and a test on the proximity to identified clouds. We have also investigated the effect of adding a ray tracing test to reinforce the penalisation of zones most probably affected by cloud shadows. A description of the Sentinel-2 data used and the domain of study is made in Section 2. The proposed methodology to detect shadows is then described in Section 3. The results and their validation are presented in Sections 4 and 5 respectively and the conclusions and future outlook are presented in Section 6.

2. Data used

2.1. Satellite data

Sentinel-2 with the MSI payload (S2/MSI) was launched by European Space Agency (ESA) in June 2015. The S2/MSI sensor has 13 bands in the visible ranges with spatial resolution ranging from 10 to 60 m, and a 20 m resolution in the red to near-infrared (NIR) bands. The S2/MSI level 1C (L1C) products were obtained from the Copernicus Open Access Hub, as orthorectified 100 km × 100 km² tiles (ortho-images in UTM/WGS84 projection). The L1C products provide per-pixel Top Of Atmosphere (TOA) reflectances with the parameters to transform them into radiances.

The S2/MSI L1C tiles were processed with ACOLITE (v20180925, Dark Spectrum Fitting) to generate level 2 (L2) remote sensing reflectance $\rho_w(\lambda)$ products. ACOLITE performs the atmospheric correction using the "dark spectrum fitting" approach for coastal and inland water applications (Vanhellemont and Ruddick, 2018). Non-water pixels (i.e. land, cloud contamination) are flagged using the shortwave infrared (SWIR) band following the criteria: $\rho_w(1610) > 0.0215$. An additional cirrus cloud detection is performed based on the 1375 nm spectral band using $\rho_w(1375) > 0.005$. SPM concentration (gm^{-3}) products were generated using the algorithm of Nechad et al. (2010):

$$SPM = \frac{A^\rho \rho_w}{1 - (\rho_w/C^\rho)} + B^\rho \qquad (1)$$

where A^ρ (gm^{-3}), B^ρ (gm^{-3}) and C^ρ (unitless) are constant values which mainly depend on the water inherent optical properties and were set to 610.94, 0 and 0.2324 respectively for the 665 nm spectral band. For the satellite data application B^ρ is set to zero because the satellite sensor and processing will probably have different measurement errors from the calibration data.

The CHL product is derived from a combination of two compatible algorithms: the O'Reilly blue-green band ratio OC3 algorithm (O'Reilly et al., 2000) and the red/Near-Infrared band ratio Gons algorithm (Gons et al., 2002, 2005). The OC3 algorithm was designed for open ocean
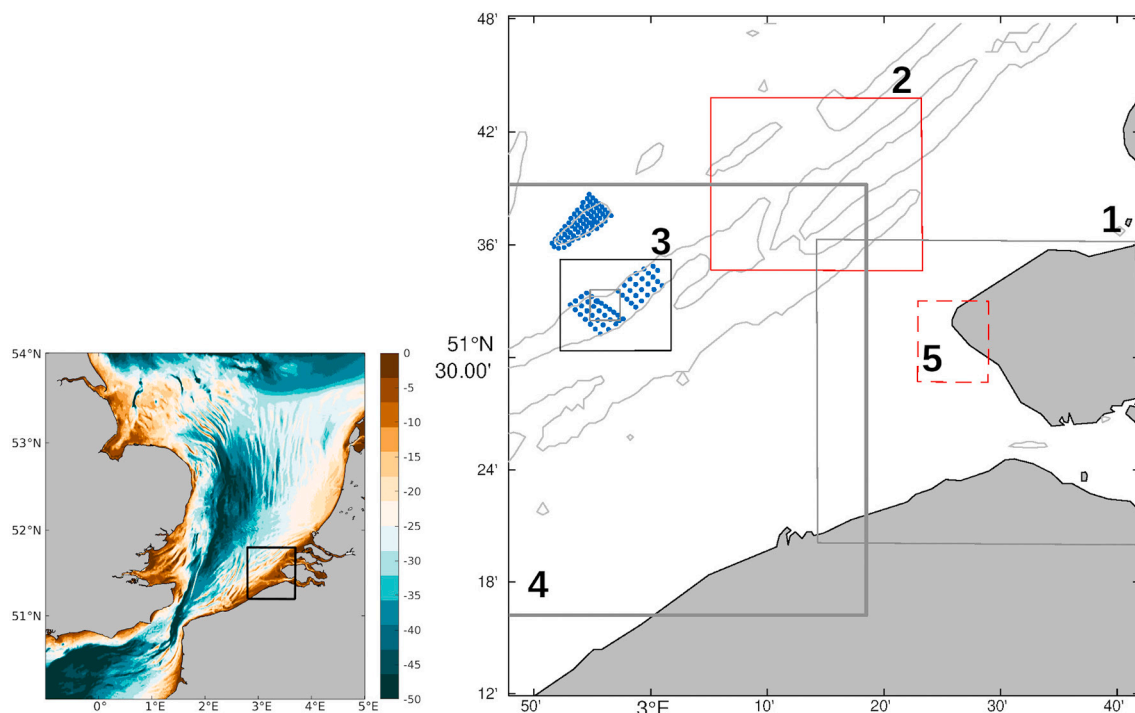

Fig. 1. Domain of study, containing the Belgian Coastal Zone and part of the southern North Sea. Isobaths for 20 m depth are shown, as well as the location of the windmill parks (in blue). The different squares show the position of the subdomains given as examples in the Results Section 4.

waters and the Gons algorithm for eutrophic and turbid coastal waters. Pixel-based dynamic switching between these algorithms is performed based on best suited algorithm/water type combination as described in Van der Zande et al. (2019).

2.2. Manual cloud shadow identification

Cloud shadows were manually identified for validation purposes by a human operator using the RGB images for the S2/MSI scenes for 29 April 2017 and 4 August 2017 on the Belgian Coastal Zone. The RGB images were imported in GIMP (v2.10.2) and cloud shadows were selected using the 'Bucket Fill' tool enabling an automated selection of pixels based on the selected foreground colour. The number of filled pixels depends on the Fill threshold. The fill starts at the point selected by the operator and spreads outward until the colour value becomes "too different" from the selected pixel. The optimal threshold was selected through trial and error to obtain the best coverage of the considered cloud shadow. While this approach worked well in turbid waters and opaque clouds casting clearly defined shadows on the scattering waters, it was more difficult in clear absorbing waters where the colour difference caused by clouds was minimal compared to clear water pixels. In these conditions it was difficult to manually identify the borders of the cloud shadow. Similarly, shadows cast by thin clouds are blurry and difficult to clearly define. The manual identification of the cloud shadows took 10 to 15 h per image highlighting the need for an automated detection approach.

2.3. Study areas

The cloud shadow detection is first applied to the Belgian Coastal Zone (Fig. 1) in the southern North Sea. This zone comprises high SPM near the coast and a strong offshore decreasing gradient. The high SPM concentration near the coast is due to the discharge of the Scheldt, Rhine and Meuse rivers in the Scheldt-Rhine estuary (located in the eastern part of the domain), and therefore the temporal variability of SPM concentration is largely dependent on river discharge. The North Sea shelf is very shallow, with an average depth of 30 m in the large domain shown in Fig. 1, and an average depth of 15 m in the domain of study. Tidal currents therefore also play an important role in determining SPM concentration and dynamics, through deposition and resuspension.

A second domain of study is the Venice area. This region presents in general lower values of SPM although river discharge results in high SPM values intermitently. The amount of clouds is lower than in the Belgian Coastal Zone, and shadows are less prominent. This region will be used therefore to test whether our shadow detection approach can deal with these characteristics.

3. Detection of shadows: method description

The shadows in high spatial resolution datasets like S2/MSI can have very different sizes, and represent therefore a multi-scale problem. Shadows can have all forms and sizes: from the large cumulus clouds casting shadows that can be several kilometers wide, to the thin and
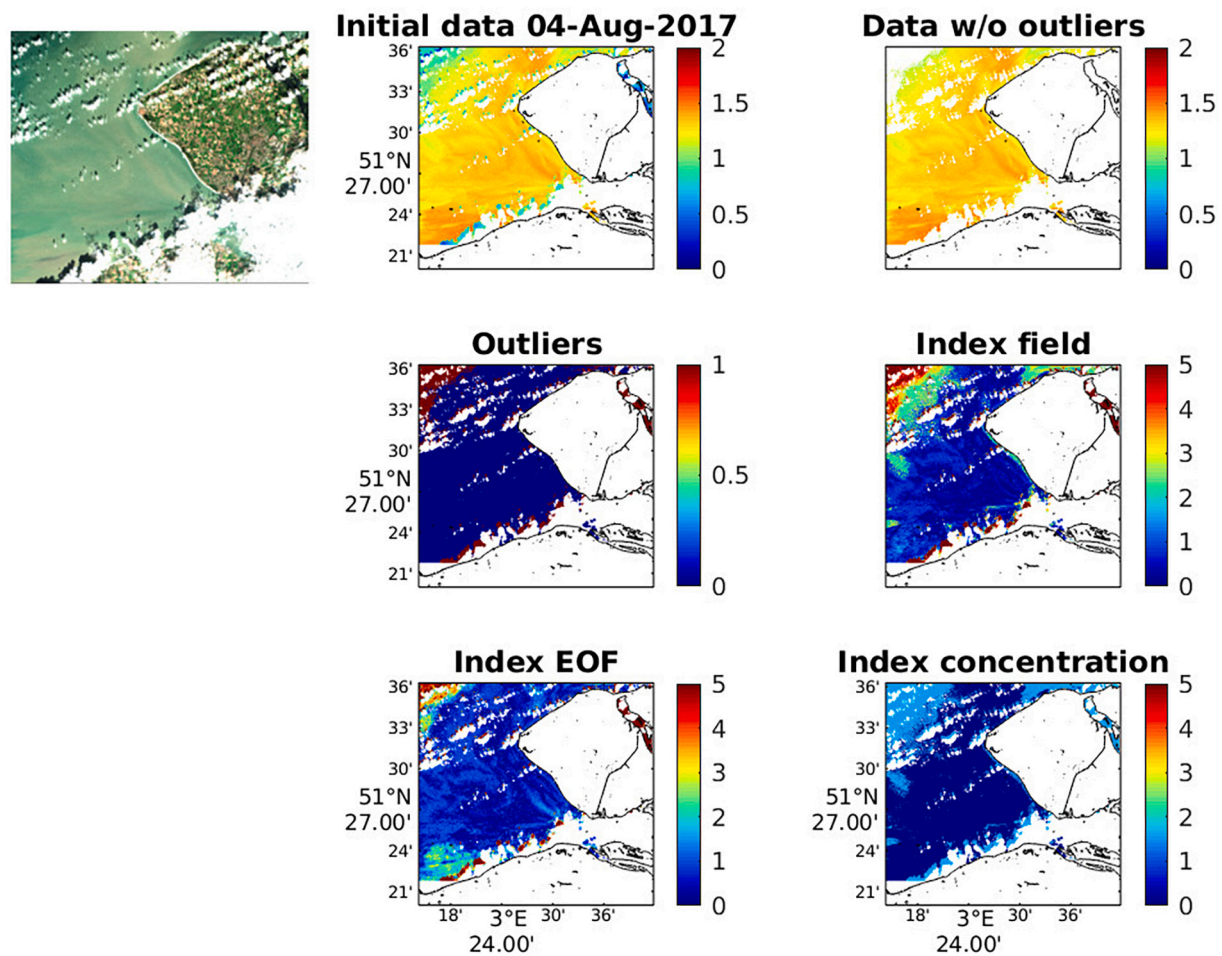

Fig. 2. Shadow detection example on 4 August 2017 (RGB view in the top left insert). From bottom to top: bottom left and right panels show the result of O_{EOF} and O_{conc} respectively. The middle right panel show the O_{final} index, from which a threshold of 2 is applied to determine which pixels are shadows. The final shadow/non-shadow mask is shown in the middle left panel. Top left panel shows the initial SPM data, with very low values corresponding to cloud shadows. Top right panel shows the final image after shadows have been removed.

relatively small windmill masts, which are less than 100 m long.

In order to detect shadows at different spatial scales, a set of different tests are performed on the data. These tests build on the outliers detection approach described in Alvera-Azcárate et al. (2012, 2015), in which outliers were detected in medium spatial resolution data (sea surface temperature from AVHRR and turbidity from SEVIRI, respectively). In this approach, individual pixels with a behavior distinct from their neighboring pixels were targeted, but given the spatial extension of cloud shadows, these cannot be detected using directly the approach in Alvera-Azcárate et al. (2012, 2015). The detection of shadows in high resolution data needs the addition of some tests adapted to the problem. The tests are described as follows:

- EOF index, O_{EOF}: A first test determines the departure of each pixel from an EOF basis calculated from the data being analysed. This EOF basis is calculated using DINEOF (Beckers and Rixen, 2003; Alvera-Azcárate et al., 2005) to overcome the problem of missing data. The EOF basis is truncated by retaining only the modes that minimise the error of the reconstruction. Transient and localized features like shadows are therefore not part of the EOF basis and can be identified by its departure from it. The mean absolute difference between an original pixel and the estimation obtained by the truncated EOF basis is calculated. This test provides a departure index with values starting from zero (no difference between a pixel and the EOF basis at that point) and with an unbounded positive value for pixels differing from the EOF basis.

- Proximity index, O_{prox}: Typically, pixels surrounding clouds are more likely to exhibit a shadow in their vicinity. This test gives a value of 1 to pixels immediately surrounding an already missing value (cloud, land, bad data masked for quality reasons) and zero otherwise. This test can be applied iteratively to reach further away from the cloud or land edges.

- Concentration test, O_{conc}: The presence of shadows in ocean colour variables is always associated to low values of the variable being analysed relative to the surrounding clear water pixels. However, as already mentioned, these are still within the range of plausible values, and cannot be detected as outliers by applying a fixed threshold. To overcome this, a varying threshold is instead applied, which depends on the amount of missing data in each individual image and the quantile distribution of the values of the variable used (SPM concentration or CHL in this case). The higher the percentage of missing data (%MD) of a given image, the higher the quantile below which data are considered suspect. The concentration test is only applied when $\%MD > 20\%$:

$$\text{data} > Q_{\%\text{MD}/100} \rightarrow O_{conc} = 0; (\text{else } O_{conc} = 1) \qquad (2)$$

The rationale behind this setting is that, the higher the percentage of missing data on a given image (and therefore of clouds), the more probable that a given clear pixel is a shadow. As an example, if a given image has 10% of missing data, and the 10th quantile for all the values of that same image is 0.3, then all pixels with an SPM value smaller than 0.3 gm^{-3} will be given a $O_{conc} = 1$. If that same image has 15% of missing data, and the 15th quantile is 0.47, then all pixels with an SPM value
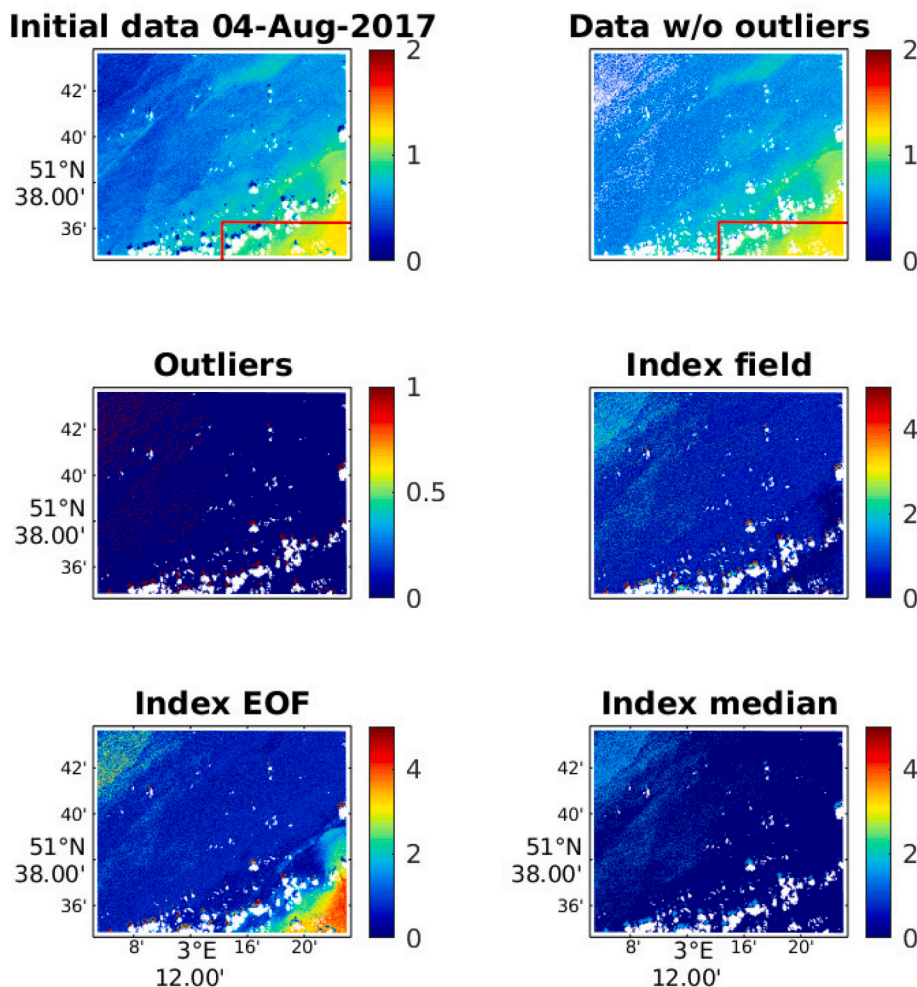

Fig. 3. Shadow detection example on 4 August 2017 in an open domain containing the northwest corner of Fig. 2 (shown by the red line). From bottom to top: bottom left and right panels show the result of O_{EOF} and O_{median} respectively. The middle right panel show the O_{final} index, from which a threshold of 2 is applied to determine which pixels are shadows. The final shadow/non-shadow mask is shown in the middle left panel. Top left panel shows the initial SPM data, with very low values corresponding to cloud shadows. Top right panel shows the final image after shadows have been removed. (For interpretation of the references to colour in this figure legend, the reader is referred to the web version of this article.)
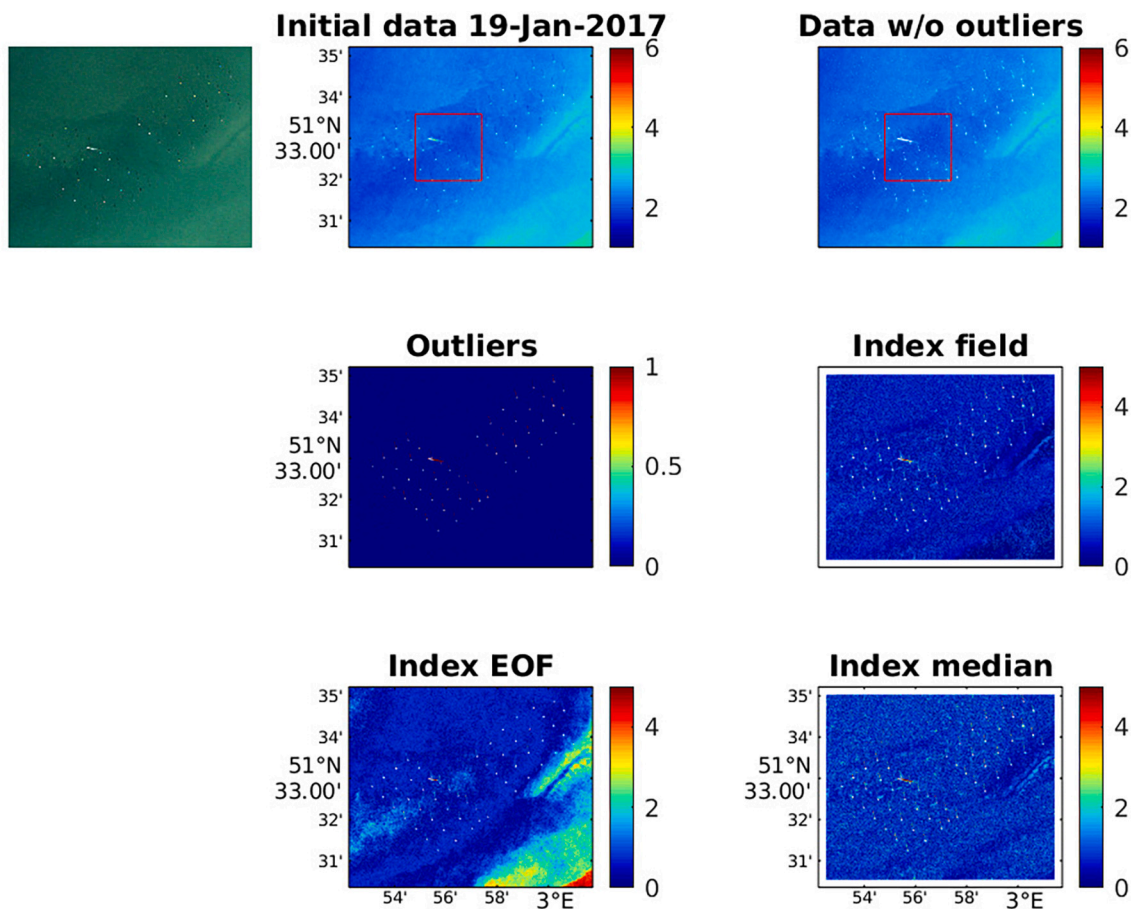
Fig. 4. Shadow detection example on 1 January 2017 in the C-Power offshore windmill park (RGB view in the top left insert). From bottom to top: bottom left and right panels show the result of O_{EOF} and O_{median} respectively. The middle right panel show the O_{final} index, from which a threshold of 2 is applied to determine which pixels are shadows. The final shadow/non-shadow mask is shown in the middle left panel. Top left panel shows the initial SPM data, with very low values corresponding to windmill shadows, and very large values associated with a ship wake. Top right panel shows the final image after shadows and wake have been removed. Red squares in the top row indicate the domain shown in Fig. 5. (For interpretation of the references to colour in this figure legend, the reader is referred to the web version of this article.)

smaller than 0.47 gm^{-3} will be given a $O_{conc} = 1$.

- Median test, O_{median}: the difference between a given pixel and a local median calculated over a 30×30 box, normalized by the mean absolute deviation calculated over the same domain, is calculated. Departures from this median are penalised. This test is only applied if the percentage of missing data is lower than 20%, as the computational cost is high and this test is most efficient in detecting very small shadows on clear days (like windmill mast shadows). The size of the box has been chosen to concentrate in small-scale features.

An index O_{final} is finally calculated as the weighted sum of the three mentioned tests:

$$O_{final} = W_1 O_{EOF} + W_2 O_{prox} + W_3 O_{conc} \tag{3}$$

with W_1, W_2 and W_3 the weights applied to each test. These weights can change depending on the data and the objectives, and the specific values used in this work will be presented in Section 4. In the case of having less than 20% of missing data in a given image, the concentration test O_{conc} is substituted by the median test O_{median}:
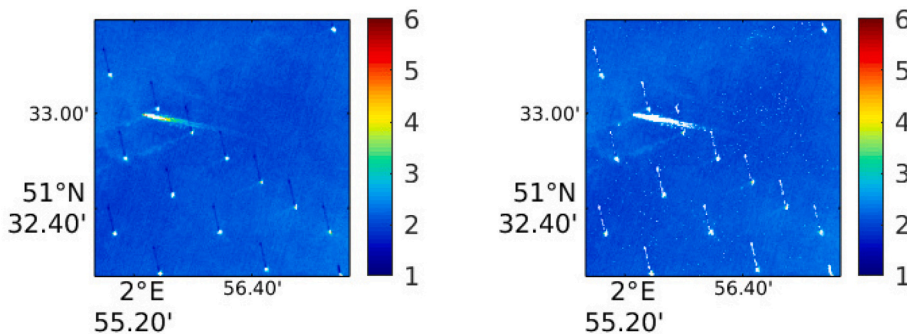

Fig. 5. Detail of the red insert of Fig. 4. Left panel shows initial SPM and right panel shows SPM after removal of shadows and other suspect data, as the ship wake. (For interpretation of the references to colour in this figure legend, the reader is referred to the web version of this article.)

$$O_{final} = W_1 O_{EOF} + W_2 O_{prox} + W_4 O_{median} \qquad (4)$$

All weights can be adjusted to the characteristics of the variable and region of interest.

An additional test can be added, in line with other existing cloud shadow detection methods, to estimate the probable location of the shadow given the position of a cloud. A ray tracing approach has been adopted, and can be described as follows:

- Ray tracing test, O_{ray}: For every pixel of the scene, we compute the position of the sun in the sky using the Julia package AstroLib. We assume that the altitude of the clouds is known and constant. The cloud layer is represented by a binary mask (0 clear sky and 1 covered sky). We computed the ray connecting a given pixel and the sun and then determined where this ray would intersect the cloud layer. If the nearest point to this intersection is a cloud, then the pixel has a shadow index of 1. Otherwise it has an index of 0.

We have used the ray tracing test by establishing a top of the cloud height of 1.5 km, which is of course not always the case. However, the ray tracing test is used only to provide a probable area of suspicious pixels, and it is most useful when thin and scattered clouds are present. The combination of the four tests and their weights determines if a pixel is shadowed or not. If the ray tracing test is applied, it is added to the previous one: $O_{final} = O_{final} + O_{ray}$.

4. Results

4.1. Detection of cloud shadows in the Belgian Coastal Zone

The shadow detection approach was applied to the 2017 S2/MSI data

described in Section 2. Given the very large size of S2/MSI data, the DINEOF reconstruction was applied to subsets of data, covering each 1/4th of the domain shown in Fig. 1. Examples of results in some of these subsets are shown here.

The specific weight of each subtest described in Section 3 was determined first by establishing which tests had a larger impact in the detection of shadows. The truncated EOF basis used to calculate O_{EOF} consisted of 3 EOFs (determined by cross-validation by DINEOF). For images with more than 20% of missing data, O_{conc} and O_{EOF} played the largest roles, and for images with less than 20% of missing data, it was O_{median} that best helped detecting shadows. Given this, and after trying several combinations, the following weights were used:

- More than 20% of missing data: $W_1 = 0.8$; $W_2 = 0.2$; $W_3 = 0.2$
- Less than 20% of missing data: $W_1 = 0.2$; $W_2 = 0.2$; $W_4 = 0.8$

The level above which a pixel is classified as shadow was fixed at 2 after some trials. Therefore, it was decided that pixels providing a value of 1 in the O_{conc} test, when more than 20% of missing data are present, are automatically classified as shadow. The O_{EOF} and O_{prox} tests help in finding some other pixels that are not correctly classified as shadow by the O_{conc} test alone. In this first domain, the ray tracing test was not used since it didn't have a measurable impact in the final shadow detection.

An example of shadow detection for 4 August 2017 is shown in Fig. 2, covering domain 1 as shown in Fig. 1. The amount of missing data on this day is 25%. The cloud shadows located along the southern coast are correctly detected, as well as the scattered shadows in the middle of the domain. There is one zone in the northwest corner of the domain that presents a large amount of false positives (i.e. pixels classified as shadows that are valid SPM data) since both O_{conc} and O_{EOF} classify these
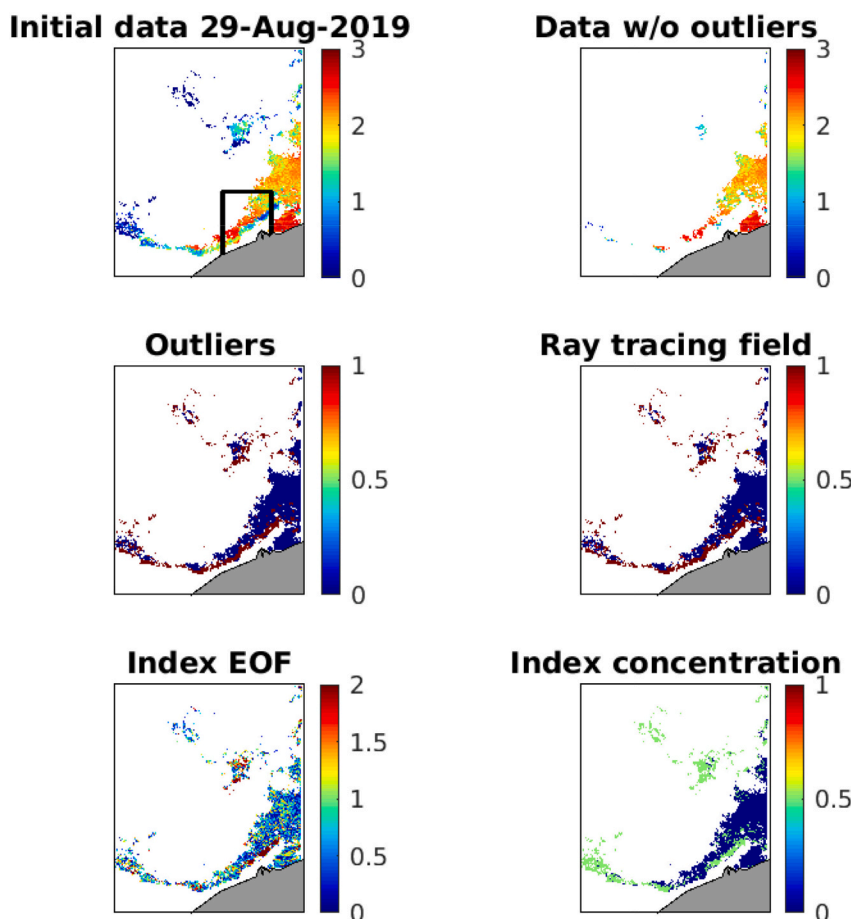

Fig. 6. Shadow detection example on 29 August 2019 in domain 4 (see RGB view top left). From bottom to top: bottom left and right panels show the result of O_{EOF} and O_{conc} respectively. The middle right panel show the O_{ray} index, with 1 to pixels affected by a cloud. The final shadow/non-shadow mask is shown in the middle left panel. Top left panel shows the initial SPM data, with very low values corresponding to cloud shadows. Top right panel shows the final image after shadows have been removed.
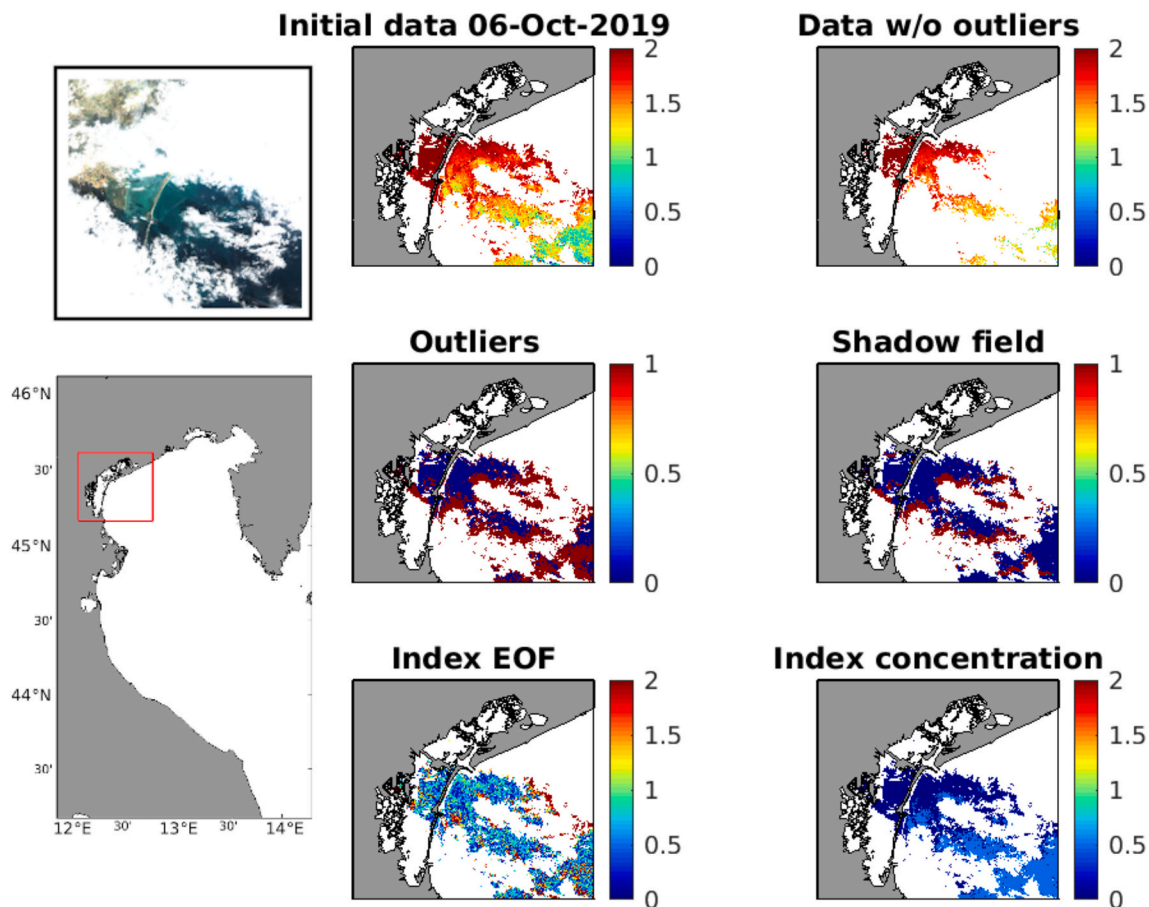
Fig. 7. Shadow detection example on 6 October 2019 in the Venice area (see insert map bottom left and RGB view top left). From bottom to top: bottom left and right panels show the result of O_{EOF} and O_{conc} respectively. The middle right panel show the O_{ray} index, with 1 to pixels affected by a cloud. The final shadow/non-shadow mask is shown in the middle left panel. Top left panel shows the initial SPM data, with very low values corresponding to cloud shadows. Top right panel shows the final image after shadows have been removed.

pixels as suspect. This zone is characterized by low values of SPM, which suggests that the accuracy of the shadow detection can be improved if the detection of shadows for that zone would be made separately, for example by determining a domain of open waters, with low values of SPM.

To test this idea, an open waters domain containing the northwestern corner of Fig. 2 is used to test if the detection of shadows is improved in that corner. Fig. 3 shows the shadow detection in domain 2 (Fig. 1), with the same tests as in Fig. 2 except for O_{conc} test which is replaced by the O_{median}, as the amount of missing data in domain 2 for 4 August is of 4%. It can be seen that the cloud shadows are now more accurately detected in the overlapping corner. The approach presented is therefore able to work in domains with lower SPM concentration values, where the shadows are not so clearly visible. A careful compositing to reunite all subscenes after shadow detection is of course needed.

4.2. Detection of windmill shadows

The presence of shadows from other sources than clouds is also visible in high spatial resolution satellite data. Offshore windmill farms are being developed quickly in many places around the globe, including the North Sea. Our domain of study contain three farms (either finished or under construction): Norther, C-Power and Northwind. The shadow detection has been applied to a domain containing the C-Power wind farm (domain 3 in Fig. 1), and the results on a very clear day (19 January 2017, with 0% of missing data) are shown in Fig. 4. In this case, as the amount of missing data is smaller than 20%, the O_{conc} test is replaced by

the O_{median} test. The shadows of the windmills are correctly detected by our approach. The wake of a ship crossing the wind farm results in erroneous high SPM concentration values, and these pixels are also detected as shadows. Since our approach can also detect features that are anomalous with respect to their surroundings, the detection of such erroneous data is also possible.

A detail of this figure is shown in Fig. 5, in which the detection of the windmill masts shadows is more clearly seen. This figure also shows that the turbid wakes created by the current flowing through the windmill masts (e.g. Vanhellemont and Ruddick, 2014), in a west-southwest direction from the masts, are (correctly) not detected as anomalous, contrary to the ship wake.

4.3. Shadow detection in chlorophyll data in the Belgian Coastal Zone

In order to test the accuracy of the shadow detection in a different setting, a test has been made using CHL data in 2019 in domain 4 of Fig. 1. The dataset used consists of 77 images spanning from 9 January 2019 to 2 December 2019 (images that have more than 96% of missing data have been removed). After realising some tests with different weights for each of the subtests, it was decided that the same combination of tests (i.e. $W_1 = 0.8$; $W_2 = 0.2$; $W_3 = 0.2$ for more than 20% of missing data) led to satisfying results. The ray tracing test was also used in this example, since we observed the presence of thin and scattered clouds. The threshold to decide whether a pixel is a cloud shadow or not was set to 1.5 (instead of 2 with SPM). While we have kept the same values as the previous examples, these need to be adjusted to the
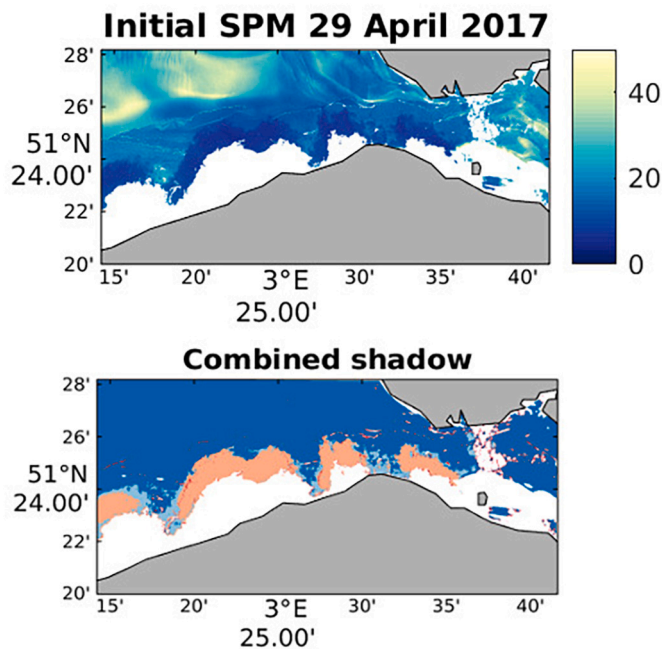
Fig. 8. Cloud shadow detection on 29 April 2017. Top panel shows SPM values, with low values (dark blue) due to shadows, and clouds in white. Bottom panel shows pixels detected as cloud both manually and by the present methodology (pink), pixels detected manually but not by our method (light blue) and pixels detected by our method but not manually (red). (For interpretation of the references to colour in this figure legend, the reader is referred to the web version of this article.)

variable and domain of study. An example on 29 August 2019 is presented in Fig. 6, with all the subtests as in previous examples. Shadows are generally well detected, and the addition of ray tracing is useful for some shadows near the southwest corner.

4.4. Shadow detection in SPM data on the Venice area

The shadow detection approach has been also tested in a different region. S2/MSI SPM data in the Venice area from 2019 were chosen, as this region presents very different values in SPM than the Belgian Coastal Zone. The weights were again maintained as in the 2 previous tests, adding the ray tracing test as well. The threshold to classify a pixel as shadow or not was set to 2. An example on 6 October 2019 is presented in Fig. 7, again showing that most shadows are correctly identified.

5. Validation

5.1. Cloud shadow detection in the Belgian Coastal Zone SPM dataset

In order to assess the accuracy of our approach, we have selected 2 scenes in which cloud shadows have been detected manually: 29 April 2017 and 4 August 2017 in the Belgian Coastal Zone. As described in Section 2.2, shadows were detected manually along the domain of study by individually selecting all pixels identified as shadow. While this is a long and tedious work to realise, it also provides a very strict validation baseline to compare our shadow detection approach with.

An example is shown in Fig. 8 for 29 April 2017. In this case, 63% of the pixels detected manually as being shadows have been detected by our approach. The percentage of no-cloud pixels classified as shadows by our approach but not manually is 3%, and while these can be considered false positives, close inspection of the image shows that there are also pixels at the edges of clouds that might have been overlooked in the manual detection.

Two more examples are given for small scattered clouds, on 4 August 2017 (Fig. 9). First on the eastern part of the domain (domain 6, shown in the left column of Fig. 9). On this part of the domain, 85.20% of the pixels detected manually as being shadows have been detected by our approach. A 4.10% of the open-sea data (i.e. no clouds nor shadows) are classified as shadows by our approach but not manually, but again, this percentage includes false positives and pixels not detected manually but that are shadows. The second example is given for domain 2, and it is shown in the right column of Fig. 9. On this part of the domain, 75.22% of the pixels detected manually as being shadows have been detected by our approach. A 1.21% of the open-sea data (i.e. no clouds nor shadows) are classified as shadows by our approach but not manually, a percentage that includes false positives and pixels not detected manually but that are shadows. In this specific frame, close inspection of the scattered pixels detected with our approach shows they are mostly whitecaps in the initial data, and have been identified as suspect data.

5.2. Comparison with Idepix

While the comparison with manually detected shadows provides a very good frame to objectively assess the accuracy of the results, it is interesting to assess how our approach compares with other existing automated approaches for detection of cloud shadows. For the example on 4 August 2017 we can therefore assess the accuracy of our method and the accuracy obtained with Idepix, a S2/MSI cloud shadow processor developed for the SNAP (Sentinel Application Platform) software (Lebreton et al., 2016). Idepix combines the cloud mask with sun geometry to search regions of maximum probability for shadow pixels. As no cloud height is available for S2/MSI data, a maximum cloud height is predetermined as a function of latitude. Within the projected region of potential cloud shadow, the cloud mask is shifted towards the surface reflectance minimum along the illumination path. These pixels are flagged as IDEPIX_CLOUD_SHADOW. Additionally, pixels within the potential shadow area are clustered based on surface reflectances and the darkest cluster is flagged as IDEPIX_CLUSTERED_CLOUD_SHADOW. Both flags were combined to a single cloud shadow flag in this study.

The whole domain for 4 August 2017 is shown in Fig. 10, together with the shadows detected manually, with Idepix and with our approach. It can be seen that our approach shows more scattered pixels that have been detected as shadows but do not appear in the manual mask (especially in the southwest corner). On the other hand, Idepix seems to have overestimated the shadow for the large cloud situated in the southwest, and presents also some scattered clouds near the coast not detected manually. In order to assess the accuracy of each method, we will zoom in these two places, marked with a square in Fig. 10.

Fig. 11 shows the first zoomed image. Compared with the manual shadow mask, our approach detects 82.30% of the shadows, with 9.70% of false positives, which appear to be scattered shadows north of the cloud associated with low concentration SPM values. Idepix on the other hand, has a too large cloud shadow, and compared with the manual mask it detects 65% of them. In terms of false positives in Idepix, because of the large shadow, this value goes up to 18%. The second zoom is presented in Fig. 12. Here our approach detects too few shadows, summing up to 50% of the manual shadows and 1.9% of false positives. Idepix detects 60% of the manual shadows, with 1.6% of false positives. We can see an artifact in the Idepix detected shadows in the form of a line, and again some scattered shadows for our approach.

The percentage of shadows detected in the second zoom is quite low for our approach, though Idepix also underperformed with respect to the results in the first zoom. This scene appeared as specially challenging for both approaches. Close inspection of this scene reveals that our approach failed to detect thin shadows caused by the clouds edges. A way to improve on this would therefore be to increment the shadows by two or three pixels around the detected shadows. The number of false positives would however also increase.
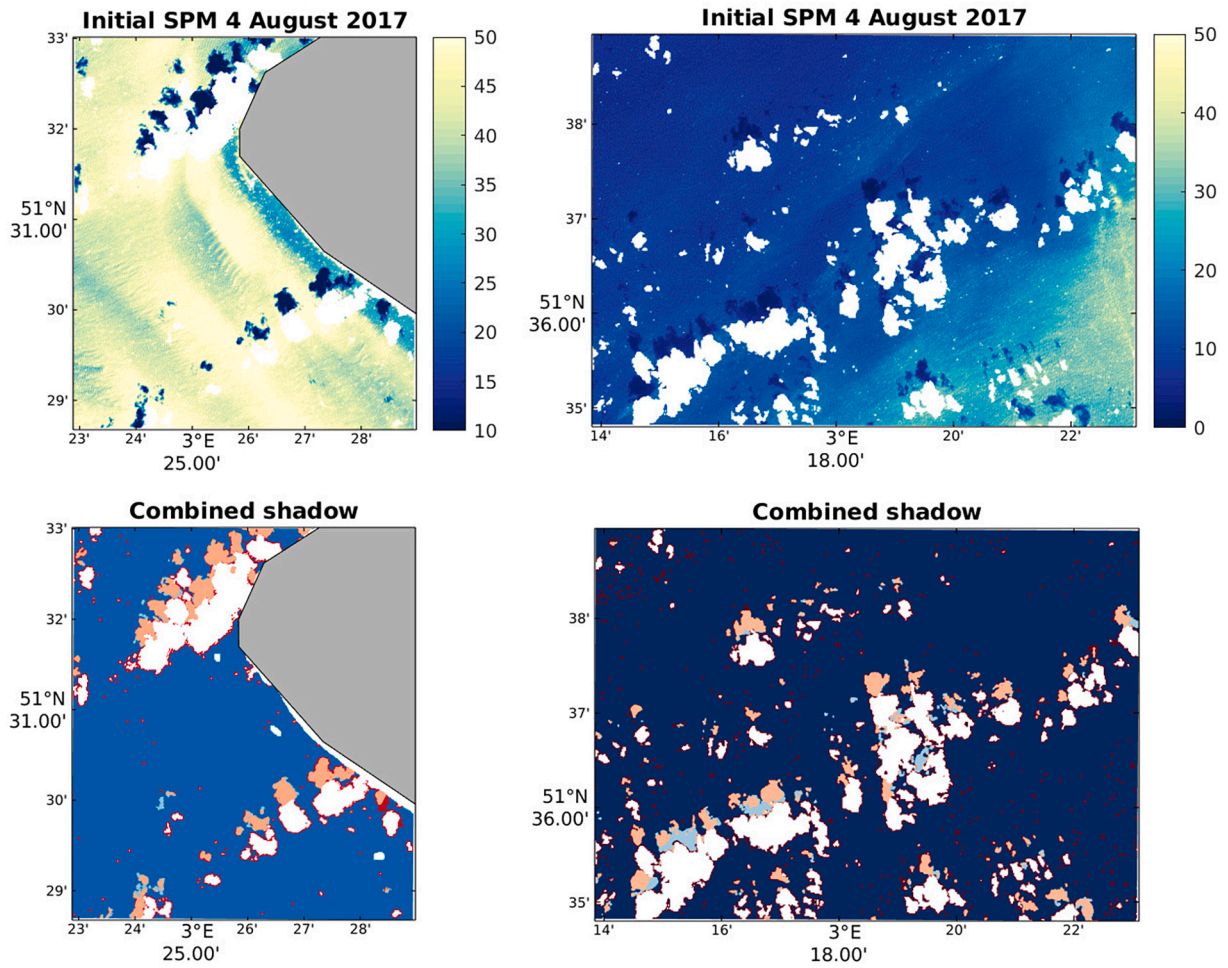
Fig. 9. Cloud shadow detection on two subdomains on 4 August 2017. Top left panel (east domain) shows SPM values, with low values (dark blue) due to shadows, and clouds in white. Bottom left panel shows pixels detected in the east domain as cloud both manually and by the present methodology (pink), pixels detected manually but not by our method (light blue) and pixels detected by our method but not manually (red, mostly at some cloud edges). Top right panel (northwest domain) shows SPM values, with low values (dark blue) due to shadows, and clouds in white. Bottom left panel shows pixels detected in the northwest domain as cloud both manually and by the present methodology (pink), pixels detected manually but not by our method (light blue) and pixels detected by our method but not manually (red, mostly at some cloud edges). (For interpretation of the references to colour in this figure legend, the reader is referred to the web version of this article.)
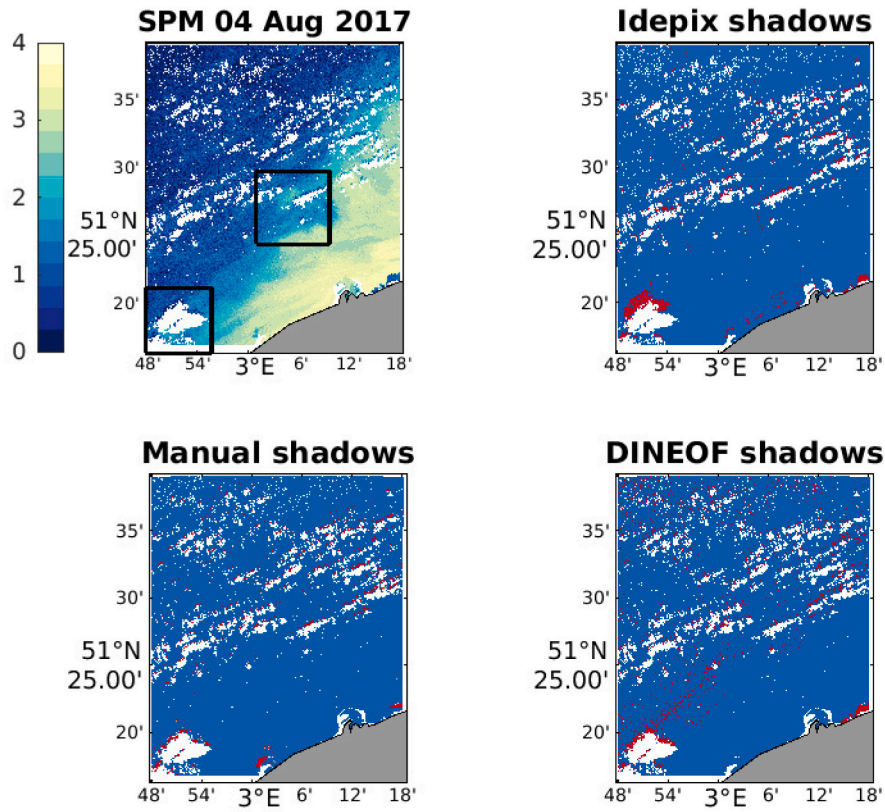
Fig. 10. Cloud shadow detection on domain 4, for 4 August 2017. Top left panel shows SPM values, with low values (dark blue) due to shadows, and clouds in white. Bottom left panel shows pixels detected as shadow manually (in red). Top right panel shows the shadows detected by Idepix, and the bottom right panel shows the shadows detected by the present method. (For interpretation of the references to colour in this figure legend, the reader is referred to the web version of this article.)
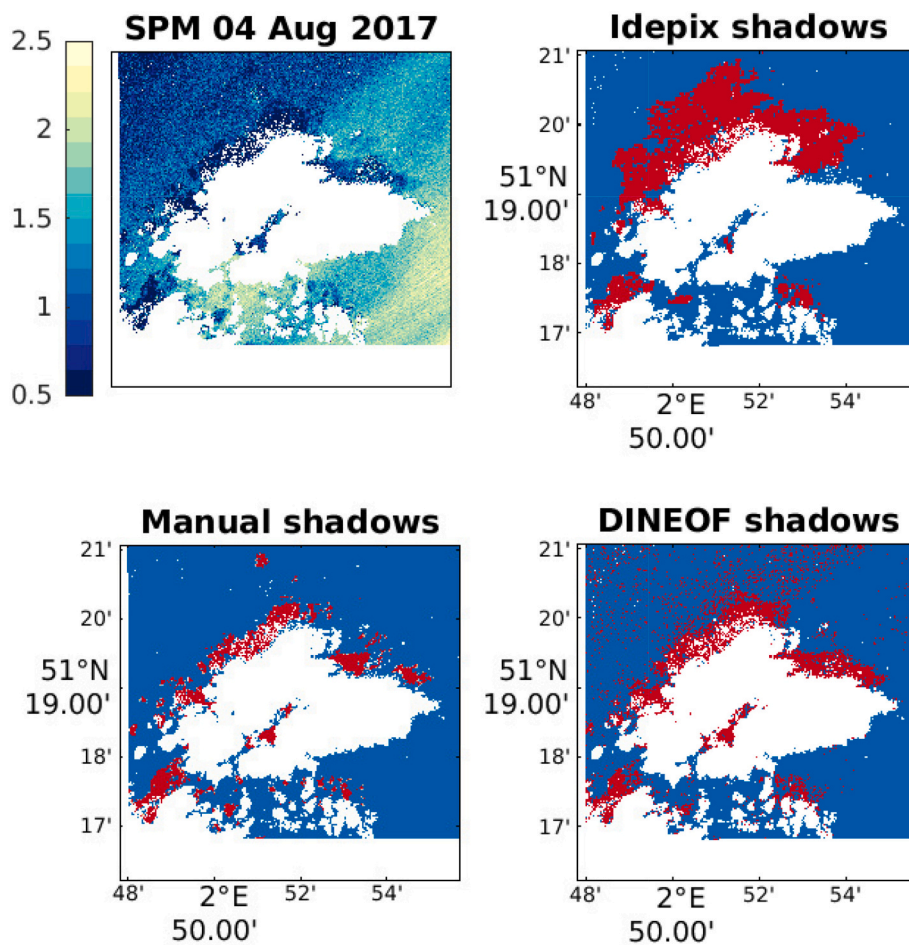
Fig. 11. Cloud shadow detection on the first zoom of domain 4, for 4 August 2017. Top left panel shows SPM values, with low values (dark blue) due to shadows, and clouds in white. Bottom left panel shows pixels detected as cloud manually (in red). Top right panel shows the shadows detected by Idepix, and the bottom right panel shows the shadows detected by the present method. (For interpretation of the references to colour in this figure legend, the reader is referred to the web version of this article.)

5.3. Chlorophyll BCZ dataset validation

For the validation of the CHL shadow detection in the Belgian Coastal Zone we have the results of our approach and from Idepix. Because none of these two can be considered the truth, it is more a comparison exercise than a validation, although visual inspection can already give a good estimate about the shadow detection accuracy of each method. First, the results of the subtests are presented in Fig. 13. It can be seen that both approaches identify most of the shadow pixels present in the left panel. The present method still has some scattered pixels detected as shadows, but on the other hand it also detects correctly that some pixels in the low left corner, close to the coast, are probably not shadow. Idepix classifies all these as shadow. If we were to consider Idepix as the truth, our approach detects 70.5% of Idepix shadows, and Idepix classifies as no shadow 12.5% of pixels classified as shadow in our approach.

5.4. SPM Venice dataset validation

For the SPM dataset in Venice, a comparison with Idepix is also done. The results are presented in Fig. 14 for Idepix and our approach. This case, with a large cloud cover over most of the scene, seemed to be more difficut for Idepix, which ended up classifying large zones as shadow, while clearly these are not shadowed in the left panel. Idepix took more than 20 h of computation for this single scene. Our approach looks closer to what the actual shadows are. Comparing again the percentage of pixels detected as shadows in each technique, there are 54% of Idepix shadows that have been classified as shadows by our approach, and 29% of shadows in our approach that have not been classified as shadows in Idepix.

6. Discussion and conclusions

A method to detect shadows in high spatial resolution ocean satellite data has been described. The method detects shadows of various sizes, from large clouds down to the masts of offshore windmills. Large cloud shadows can affect the quality of the images and hence the analysis derived from them, but also at the mast-scale size, undetected shadows can have a net influence in studies aiming at assessing the impact of offshore windmill parks in the total quantity of suspended matter.

The methodology proposed is based on a series of tests applied directly to the physical variables derived from the satellite measured radiances. It does not depend therefore in the characteristics of the satellite sensor (wavebands measured) and can be applied to any satellite. The data used in this work was suspended particulate matter (SPM) and chlorophyll (CHL) measured by Sentinel-2, and two domains (Belgian Coastal Zone and Venice) and periods (2017 and 2019) were analysed. The tests include a departure from a truncated EOF basis calculated from a time series of images (large departures are penalised), a threshold test (low values are penalised), a proximity test (pixels adjacent to missing data are penalised), and a median test in images with low percentage of missing data (departures from local median are penalised). A ray tracing test can also be used, which calculates the path between each pixel and the Sun to determine if there is a cloud projecting a shadow. This test has proved to be useful in the presence of thin and scattered clouds, and therefore we recommend its use along the rest of the tests. These various tests can be weighed differently depending on the dataset used, and the threshold above which data are discarded can also be adjusted.

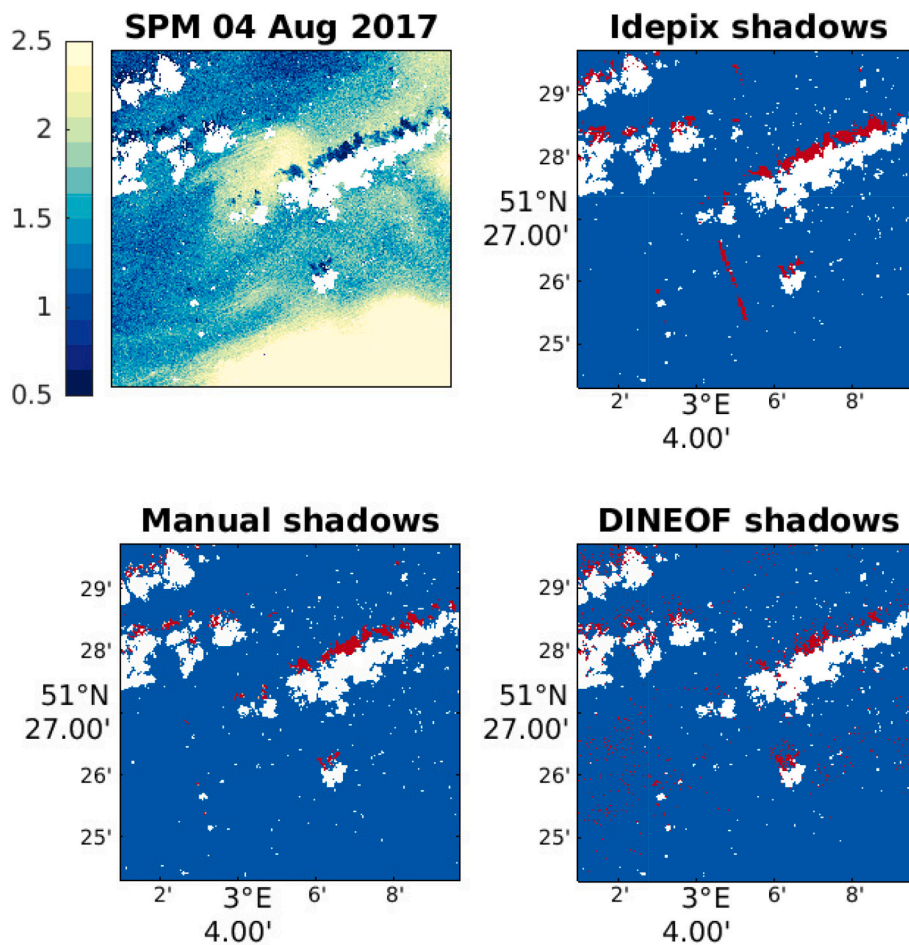The results were compared to manually selected cloud shadows, and

Fig. 12. Cloud shadow detection on the second zoom of domain 4, for 4 August 2017. Top left panel shows SPM values, with low values (dark blue) due to shadows, and clouds in white. Bottom left panel shows pixels detected as shadow manually (in red). Top right panel shows the shadows detected by Idepix, and the bottom right panel shows the shadows detected by the present method. (For interpretation of the references to colour in this figure legend, the reader is referred to the web version of this article.)
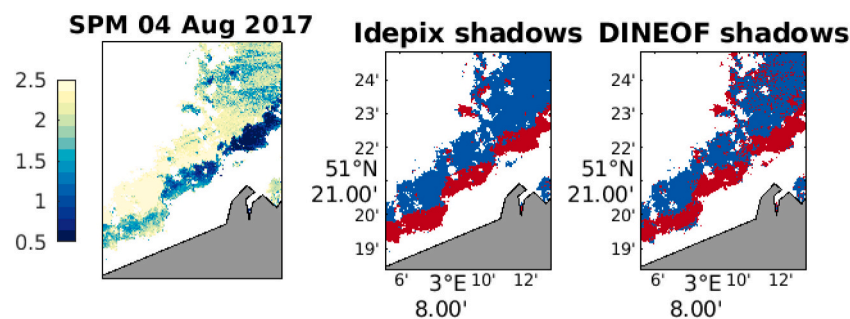

Fig. 13. Cloud shadow detection on CHL data on 29 August 2019, in the domain indicated by a square in Fig. 6. Left panel: initial CHL data. Center panel: pixels identified by Idepix as shadows (red). Right panel: pixels identified by Idepix as sadows (red). (For interpretation of the references to colour in this figure legend, the reader is referred to the web version of this article.)
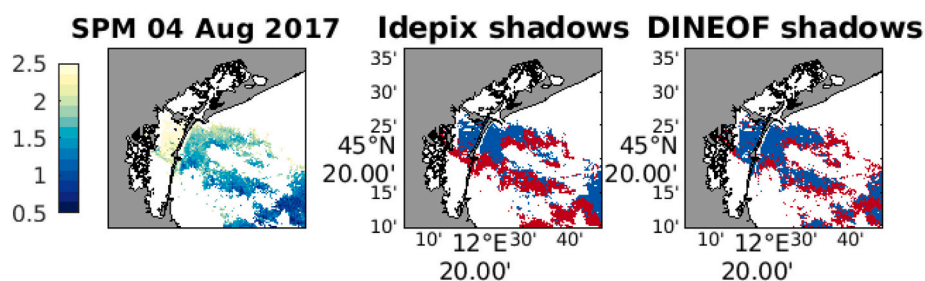

Fig. 14. Cloud shadow detection on CHL data on 6 October 2019. Left panel: initial CHL data. Center panel: pixels identified by Idepix as sadows (red). Right panel: pixels identified by Idepix as sadows (red). (For interpretation of the references to colour in this figure legend, the reader is referred to the web version of this article.)

overall a good accuracy is achieved in detecting shadows. The presence of false positives were due mainly to scattered pixels classified as shadow, and are probably low values penalised by the concentration test. Other sources of false positives were anomalous data present in the image but not due to the presence of clouds. The proposed method, as it penalises anomalous data independently of their absolute value, also detects wrong high SPM values associated with the wake of a ship, and whitecaps. These features are penalised by the EOF test.

A comparison with another shadow detection technique, Idepix, has been also performed. Depending on the frame, either Idepix or our approach performed better, compared to the manually detected pixels. Idepix seemed to overclassify possible shadow pixels, flagging large areas which are visibly not shadows. Our approach presents scattered pixels, not associated with a cloud, classified as shadows. Detecting too large shadows, as in Idepix, results in large areas being flagged out, which makes subsequent uses of the data more difficult. Scattered pixels on the other hand may have a smaller impact on the potential use of the data afterwards, as these scattered points are easier to interpolate, and do not obscure totaly large zones of valid data. In our tests we have observed a tendency for Idepix to overestimate cloud shadows, and an accuracy of 60–65%.

In our proposed method, all the tests and the final detection are based on a series of thresholds that can be adapted to provide more or less strict shadow detection. Stronger thresholds will provide a larger detection accuracy, but more false positives will be also present in the final dataset. The user can assess the thresholds best suited to their application and domain of study.

Declaration of Competing Interest

None.

Acknowledgments

References

Alvera-Azcárate, A., Barth, A., Rixen, M., Beckers, J.-M., 2005. Reconstruction of incomplete oceanographic data sets using empirical orthogonal functions. Application to the Adriatic Sea surface temperature. Ocean Model. 9, 325–346. https://doi.org/10.1016/j.ocemod.2004.08.001.

Alvera-Azcárate, A., Sirjacobs, D., Barth, A., Beckers, J.-M., 2012. Outlier detection in satellite data using spatial coherence. Remote Sens. Environ. 119, 84–91.

Alvera-Azcárate, A., Vanhellemont, Q., Ruddick, K., Barth, A., Beckers, J.-M., 2015. Analysis of high frequency geostationary ocean colour data using DINEOF. Estuar. Coast. Shelf Sci. 159, 28–36.

Beckers, J.-M., Rixen, M., 2003. EOF calculations and data filling from incomplete oceanographic data sets. J. Atmos. Ocean. Technol. 20 (12), 1839–1856.

Braaten, J., Cohen, W., Yang, Z., 2015. Automated cloud and cloud shadow identification in Landsat MSS imagery for temperate ecosystems. Remote Sens. Environ. 169, 128–138.

Frantz, D., HaAŸ, E., Uhl, A., Stoffels, J., Hill, J., 2018. Improvement of the Fmask algorithm for Sentinel-2 images: separating clouds from bright surfaces based on parallax effects. Remote Sens. Environ. 215, 471–481.

Gons, H.J., Rijkeboer, M., Ruddick, K.G., 2002. A chlorophyll-retrieval algorithm for satellite imagery (medium resolution imaging spectrometer) of inland and coastal waters. J. Plankton Res. 24 (9), 947–951.

Gons, H.J., Rijkeboer, M., Ruddick, K.G., 2005. Effect of a waveband shift on chlorophyll retrieval from meris imagery of inland and coastal waters. J. Plankton Res. 27 (1), 125–127.

Goodwin, N., Collett, L., Denham, R., Flood, N., Tindall, D., 2013. Cloud and cloud shadow screening across Queensland, Australia: an automated method for Landsat TM/ETM+ time series. Remote Sens. Environ. 134, 50–65.

Huang, C., Thomas, N., Goward, S., Masek, J., Zhu, Z., Townshend, J., Vogelmann, J., 2010. Automated masking of cloud and cloud shadow for forest change analysis using landsat images. Int. J. Remote Sens. 31 (20), 5449–5464.

Hughes, M., Hayes, D., 2014. Automated detection of cloud and cloud shadow in single-date landsat imagery using neural networks and spatial post-processing. Remote Sens. 6 (6), 4907–4926.

Lebreton, C., Stelzer, K., Brockmann, C., Bertels, L., Pringle, N., Paperin, M., Danne, O., Knaeps, E., Ruddick, K., 2016. Cloud and Cloud Shadow Masking of High and Medium Resolution Optical Sensors-an Algorithm Inter-Comparison Example for Landsat 8, vol. SP-740 (URL https://www.scopus.com/inward/record.uri?eid=2-s2.0-84988452215 partnerID=40 md5=3c1befe362880129108734bd9e04cbab).

Luo, Y., Trishchenko, A., Khlopenkov, K., 2008. Developing clear-sky, cloud and cloud shadow mask for producing clear-sky composites at 250-meter spatial resolution for the seven MODIS land bands over Canada and North America. Remote Sens. Environ. 112, 4167–4185.

Nechad, B., Ruddick, K., Park, Y., 2010. Calibration and validation of a generic multisensor algorithm for mapping of total suspended matter in turbid waters. Remote Sens. Environ. 114 (4), 854–866.

O'Reilly, J.E., Maritorena, S., O'Brien, M.C., Siegel, D.A., Toole, D., Menzies, D., Smith, R.C., Mueller, J.L., Mitchell, B.G., Chavez, F.P., Strutton, P., Cota, G.F., Hooker, S.B., McClain, C.R., Carder, K.L., Müller-Karger, F., Harding, L., Magnuson, A., Phinney, D., Moore, G.F., Aiken, J., Arrigo, K.R., Letelier, R., Culver, M., 2000. SeaWiFS Postlaunch Calibration and Validation Analyses, Part 3. Tech. rep., NASA Technical Memo (49 pages).

Qiu, S., Zhu, Z., He, B., 2019. Fmask 4.0: improved cloud and cloud shadow detection in Landsats 4–8 and Sentinel-2 imagery. Remote Sens. Environ. 231.

Sun, L., Liu, X., Yang, Y., Chen, T., Wang, Q., Zhou, X., 2018. A cloud shadow detection method combined with cloud height iteration and spectral analysis for Landsat 8 OLI data. ISPRS J. Photogramm. Remote Sens. 138, 193–207.

Van der Zande, D., Eleveld, M., Lavigne, H., Gohin, F., Pardo, S., Tilstone, G., Blauw, A., Markager, S., Enserink, L., 2019. Joint monitoring programme of the EUtrophication of the NOrth Sea with SATellite data user case in Copernicus marine service ocean state report. J. Oper. Oceanogr. 12 (3), 1–123.

Vanhellemont, Q., Ruddick, K., 2014. Turbid wakes associated with offshore wind turbines observed with Landsat 8. Remote Sens. Environ. 145, 105–115.

Vanhellemont, Q., Ruddick, K., 2018. Atmospheric correction of metre-scale optical satellite data for inland and coastal water applications. Remote Sens. Environ. 216, 586–597.

Zhai, H., Zhang, H., Zhang, L., Li, P., 2018. Cloud/shadow detection based on spectral indices for multi/hyperspectral optical remote sensing imagery. ISPRS J. Photogramm. Remote Sens. 144, 235–253.

Zhu, Z., Woodcock, C., 2012. Object-based cloud and cloud shadow detection in Landsat imagery. Remote Sens. Environ. 118, 83–94.

Zhu, Z., Woodcock, C., 2014. Automated cloud, cloud shadow, and snow detection in multitemporal Landsat data: an algorithm designed specifically for monitoring land cover change. Remote Sens. Environ. 152, 217–234.

Zhu, Z., Wang, S., Woodcock, C.E., 2015. Improvement and expansion of the Fmask algorithm: cloud, cloud shadow, and snow detection for Landsats 4-7, 8, and sentinel 2 images. Remote Sens. Environ. 159, 269–277.